EEG error-related potentials encode magnitude of errors and individual perceptual thresholds

Fumiaki Iwane[a,b,c,✉], **Iñaki Iturrate**[d,e], **Ricardo Chavarriaga**[d,f], **and José del R. Millán**[b,c,d, ✉]

[a]Learning Algorithms and Systems Laboratory (LASA), École Polytechnique Féderale de Lausanne (EPFL), Lausanne 1015, Switzerland
[b]Dept. of Electrical and Computer Engineering, The University of Texas at Austin, Austin, TX 78712, USA
[c]Dept. of Neurology, The University of Texas at Austin, Austin, TX 78712, USA
[d]École Polytechnique Féderale de Lausanne (EPFL), Campus Biotech, Genève 1202, Switzerland
[e]Amazon EU, Barcelona, Spain
[f]ZHAW Datalab, Zurich University of Applied Sciences, Winterthur 8401, Switzerland

Error-related potentials (ErrP) are a prominent electroencephalogram (EEG) correlate of performance monitoring, and so crucial for learning and adapting our behavior. Although there exists an agreement that ErrP signal awareness to errors, it remains poorly understood whether they encode further information. Here we report an experiment with sixteen participants during three recording sessions in which occasional visuomotor rotations of varying magnitude occurred during a cursor reaching task. We designed a brain-computer interface (BCI) to detect ErrP in single trials that provided real-time feedback to participants by changing the color of the cursor upon ErrP detection. The individual ErrP-BCI decoders exhibited good transfer across recording sessions and scalability over the varying magnitude of errors. Our results indicate that ErrPs encode not only the conscious perception of errors, but also their magnitude, in their amplitude and latency. Furthermore, a non-linear relationship between the ErrP-BCI output and the magnitude of errors predicts individual perceptual thresholds to detect rotations. The uncovered relationship is consistent with non-human primate studies, which found a similar relationship between the size of errors and simple spike activity of Purkinje cells, and we conjecture a cerebellar contribution to ErrP. Our experimental setup and findings open new avenues to probe and extend current theories of performance monitoring, which are based on response conflict tasks, by incorporating continuous human-interaction tasks as well as analysis of the ErrP complex as a whole rather than individual peaks.

Adaptive motor learning | Error-related potentials | Brain-computer interface | Magnitude of Error | Individual perceptual threshold

Correspondence: ***fumi.iwane@nih.gov and jose.millan@austin.utexas.edu***

DRAFT

Introduction

Skillful tennis players can hit and return a ball with the desired effect because of their ability to identify errors between the predicted next states and the actual ones along the trajectory, which enables them to adjust their actions seamlessly (1). However, this is a challenging task for novice players. This individual variability in our ability to detect errors of varying degrees is key for sensorimotor and adaptation learning (2, 3). While previous research has uncovered a neural correlate of performance monitoring in the human electroencephalogram (EEG) elicited by the awareness of discrete erroneous actions, the so-called error-related potentials (ErrP) (4–8), little is known about whether these potentials encode the magnitude of errors. Some previous studies have reported co-varying characteristics of the ErrP with error magnitudes (9, 10) —such as phase coherence or amplitude—, while others did not (11). A major limitation of these studies is the use of a limited number of error categories (i.e., small, medium and large) that failed to capture a continuous relationship between the magnitude of errors and the characteristics of the ErrP. Such a relationship is critical to predict our individual ability to discern errors.

Here we designed an experiment to further investigate these two open questions –namely, does ErrP encode the magnitude of errors? Can they predict the individual threshold of error awareness?–, where occasional visuomotor rotations occur during a cursor reaching task. We also developed a brain-computer interface (BCI) to detect in real time the presence or absence of ErrP in the subjects' EEG indicating a rotation of the joystick-to-cursor mapping. Critically, in our study induced errors are not constant, so as to avoid any adaptation process, and are variable in magnitude.

ErrPs are elicited when subjects perceive an erroneous action, either committed by themselves (4, 5) or by another person of agent (7, 12). The ErrP is characterized by two main deflections thought to be originated mainly from the anterior cingulate cortex (ACC) (6, 13–16), an initial error-related negativity (ERN) followed by a positive peak (Pe), observed over the frontocentral cortex. Further, a recent study found an increase of high-gamma band power along with ErrPs (17). Nevertheless, reports on the co-activating high-gamma activity are still limited and required further examination.

ErrP-BCIs have shown to enable seamless and intuitive interaction with external devices (8, 12, 18–23). Nevertheless, in these studies actions were executed at discrete steps, not continuously as required here. Some BCIs have succeeded in decoding the presence of an ErrP during a continuous task (24–27). However, these studies used experimental protocols where erroneous actions are abrupt stops of the device (24, 25), errors happen at the same moment during the interaction (26, 28), or the device fails to reach a target (27)—all extreme conditions that do not capture erroneous actions during a continuous interaction, but see Batzianoulis et al. (29). Furthermore, none of these previous studies characterized the ErrP signals as a function of the severity of the erroneous action.

We implemented a BCI system during the three recording

sessions, in which ErrPs were elicited by a visuomotor rotation while the subject was using a joystick to continuously control a computer cursor to reach a target (Fig. 1a and b). Errors (rotations of the joystick-to-cursor mapping) were induced in 30% of the trials. On the first and second recording sessions, subjects performed the cursor reaching task with three different degrees of rotation; i.e., $20°$, $40°$ and $60°$. On the third session, subjects experienced a finer range of rotations; i.e., from $3°$ to $60°$ with a step of $3°$, to characterize the ErrP over the continuous magnitude of errors. Furthermore, online continuous decoding of ErrPs were performed on the second and the third sessions in a "Plug-and-Play" manner (30) by using the data from the previous recording session. The BCI provided real-time feedback to participants by changing the color of the cursor upon ErrP detection.

Results

Behavioral results. Participants generated similar cursor trajectories across recording sessions and consistently initiated corrective actions at 0.3 s with respect to the onset of the rotation (Fig. 1c and d). The peak joystick speed was observed at 0.41, 0.40 and 0.42 s for the first, second and third session, respectively. The mean joystick speed increased along magnitude of rotation while keeping consistency over the recording sessions (Fig. 1e). Variance of averaged joystick speed was larger on the third session compared with the first and the second session due to the lower number of trials recorded for each magnitude of rotation (n = 6 ± 1 (mean $\pm$ std)). Altogether, participants had a uniform behavior over the three recording sessions, and the speed of joystick movement was a function of the magnitude of errors.

Time-frequency analysis. We observed band specific power modulation for theta [4, 8] Hz (26, 27), beta [18, 30] Hz (31, 32) and gamma [60, 90] Hz rhythms (17) (Fig. 2a and b). Theta band exhibited increased power modulation within the time window of [0.1, 0.6] s with respect to the onset of rotation. Beta and gamma band showed simultaneous modulations within the time window of [0.3, 0.8] s. While beta band power decreased, gamma band power increased when participants observed and corrected a visuomotor rotation (Wilcoxson's signed-rank test, $p < 0.001$ for all three frequency bands). Theta and gamma band activity were modulated by the magnitude of rotation, while beta band activity remained stable for the different magnitudes of rotation (Fig. 2c). Furthermore, at ERN, we observed phase-amplitude coupling between high theta ([6, 8] Hz) and gamma band, while at Pe, coupling occurred between low theta ([4, 6] Hz) and gamma band (Fig. 2d). Similar to the temporal band power, phase-amplitude coupling increased for larger magnitudes of rotation. These results confirm that theta and gamma band activity, as well as their interaction, encode the magnitude of errors, while this is not the case for beta band activity.

BCI decoding results. The amplitude of ErrPs increased and the latency of the deflections shortened as the magnitude of rotations increased (Fig. 3a and b). In the third session (Fig. 3c) it is observed the two prominent deflections in the ErrPs when participants consciously perceived the rotation (*Yes*), and similar but delayed and smaller sequential peaks when participants were not sure whether they observed the rotation (*Maybe*). Topographical representations of all trials with rotation (insets in Fig. 3a, b and c) show similar patterns in the three recording sessions; namely, focal activation of the fronto-central area, especially at 0.35 s. These results suggest that ErrPs to encode magnitude of errors in its amplitude and latency and are stable across different recording sessions.
Fig. 3d and e report both time-locked classification and online continuous decoding performance for each session (see also Table 1). Performance was similar across sessions (for different rotations in sessions 1 and 2, and balanced accuracy in the three sessions). TPR increased along with the magnitude of rotation in all conditions of classification (time-locked classification of the first and the second session and continuous classification of the second session) (Fig. 3d). The continuous classification performance (balanced accuracy) was significantly lower than the time-locked classification in the second and third sessions (Wilcoxon's signed-rank test, $p < 0.001$ for both sessions), which illustrates the challenge to perform continuous decoding of ErrPs.
During continuous decoding, presence of ErrPs were consistently detected with high temporal accuracy at around 0.850 s after the onset of rotation (Fig. 3f), which corresponds to the time window used to train the classifier, [0.2, 0.8] s (second session: 0.853 ± 0.01 s, third session: 0.846 ± 0.01 s). We then characterized the continuous relationship between the magnitude of rotations and the BCI output over the three sessions (Fig. 4). Estimated posterior probabilities of time-locked classification ranged from 0.21 (0 degrees) to 0.78 on the first two sessions and to 0.86 on the third session (60 degrees), while it ranged from 0.63 to 0.93 on the second and third sessions for continuous classification. For both, time-locked and continuous decoding, the estimated posterior probability linearly increased until $30°$, then plateaued for larger rotations. Thus, an exponential model successfully captured the modulation over the magnitudes of visuomotor rotation (r-squared = 0.975 and 0.978, for time-lock and continuous classification, respectively). These results illustrate that the ErrP-BCI can not only detect errors, but also infer the magnitude of errors.

Inferring individual perceptual thresholds. Finally, we asked weather ErrPs predict individual perceptual thresholds to detect visuomotor rotations. To answer this question, we analyzed the ErrP-BCI output in the time-locked condition of the third session. The perceptual threshold is defined as the magnitude of rotation for which participants detected only 50% of occurrences. On average, participants started to answer "Maybe" at 8 ± 3 degrees and "Yes" at 12 ± 5 degrees of rotation (Fig. 5a). Most importantly, the behavioral answer and the output of the ErrP-BCI were modulated similarly, demonstrating the transferability of the decoder over sessions and the scalability of ErrPs over the different magnitudes of rotation. Fig. 5b represents the relationship be-

DRAFT

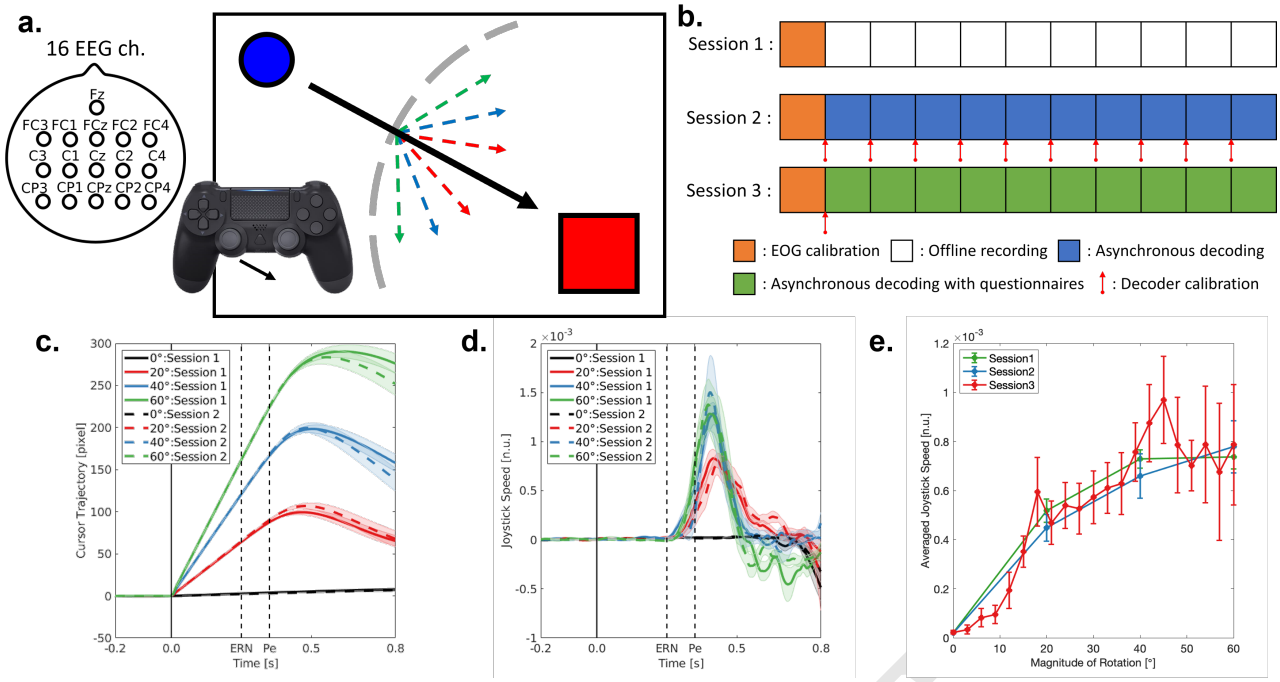

Fig. 1. Experimental protocol and behavioral results. **a.** Overview of experimental protocol. The blue circle indicates a cursor controlled by the left-joystick of a game-pad. The red square represents the goal location where participants were instructed to bring the cursor as quickly as possible. Black arrow indicates the optimal cursor trajectory (straight line) to the goal. Gray dashed line represents the boundary to induce visuomotor rotations, which was randomly defined for each trial. In a correct trial (70% of trials), no visuomotor rotation occurred. In error trials (30%) of sessions 1 and 2, visuomotor rotations could be 20° (red), 40° (blue) or 60° (green), while in session 3 rotations were from 3° to 60° with a step of 3° (lines not shown). All lines were invisible to participants during the experiment. Note that participants cannot predict occurrence of visuomotor rotations not their magnitude. **b.** Experimental timeline for each recording session. 90 s of EOG calibration data was recorded before the cursor reaching task. In session 1, participants underwent the experiment without BCI feedback. In session 2, presence of ErrPs was continuously monitored while updating the decoder after each run. In session 3, continuous decoding was performed with a fixed decoder. **c., d.** Cursor deviations from straight trajectories and joystick speed in sessions 1 and 2 (mean, continuous or dotted lines, and standard error, shaded areas). **e.** Mean joystick speed of all sessions within the time window of [0.35, 0.45] s.

Table 1. Time-locked classification and online continuous decoding performance for each recording session (mean ± SE).

a Time-locked classification

Training session	Test session	TNR of 0 °	TPR of 20 °	TPR of 40 °	TPR of 60 °	Balanced Accuracy
Session 1	Session 1	93.63 ± 1.54	57.73 ± 2.31	84.76 ± 2.13	89.74 ± 1.77	87.13 ± 1.65
Session 1	Session 2	93.84 ± 1.66	62.27 ± 2.88	87.55 ± 1.78	93.59 ± 1.77	89.16 ± 1.29
Training session	Test session	TNR of *No*	TPR of *Maybe*	TPR of *Yes*		Balanced Accuracy
Session 1 and 2	Session 3	93.13 ± 0.97	77.52 ± 4.38	89.99 ± 2.32		89.38 ± 1.38

b Continuous decoding

Training session	Test session	TNR of 0 °	TPR of 20 °	TPR of 40 °	TPR of 60 °	Balanced Accuracy
Session 1	Session 2	95.30 ± 0.76	35.37 ± 3.86	60.37 ± 5.48	71.54 ± 5.34	75.64 ± 2.51
Training session	Test session	TNR of *No*	TPR of *Maybe*	TPR of *Yes*		Balanced Accuracy
Session 1 and 2	Session 3	94.54 ± 0.97	88.11 ± 3.52	67.84 ± 4.38		80.96 ± 2.36

tween the behavioral individual perceptual threshold and the inferred individual perceptual threshold from the ErrP-BCI. Correlation analysis reveled a significant trend between the two percpetual thresholds (Spearman's $r = 0.61, p = 0.012$), while the statistical test did not reveal significant difference between the two perceptual thresholds (Wilcoxon's sign-rank test, $p = 0.41$). In summary, individual ability to detect errors was successfully inferred by characterizing the relationship between the magnitude of errors and their corresponding ErrPs.

Discussion

Our results indicate that ErrPs encode not only the conscious perception of errors (i.e., visuomotor rotations in our experimental setup) (Fig. 3c), but also their magnitude, in their amplitude and latency (Fig. 3a and b). Furthermore, classification results from session 3 demonstrates how the ErrP decoder—built from data of sessions 1 and 2 that contains only rotations of 0°, 20°, 40° or 60°—generalizes across rotations ranging from 0° to 60° with a step of 3° and across recording sessions (Fig. 4). More fundamentally, analysis of the output of the ErrP-BCI shows that ErrPs predict individ-

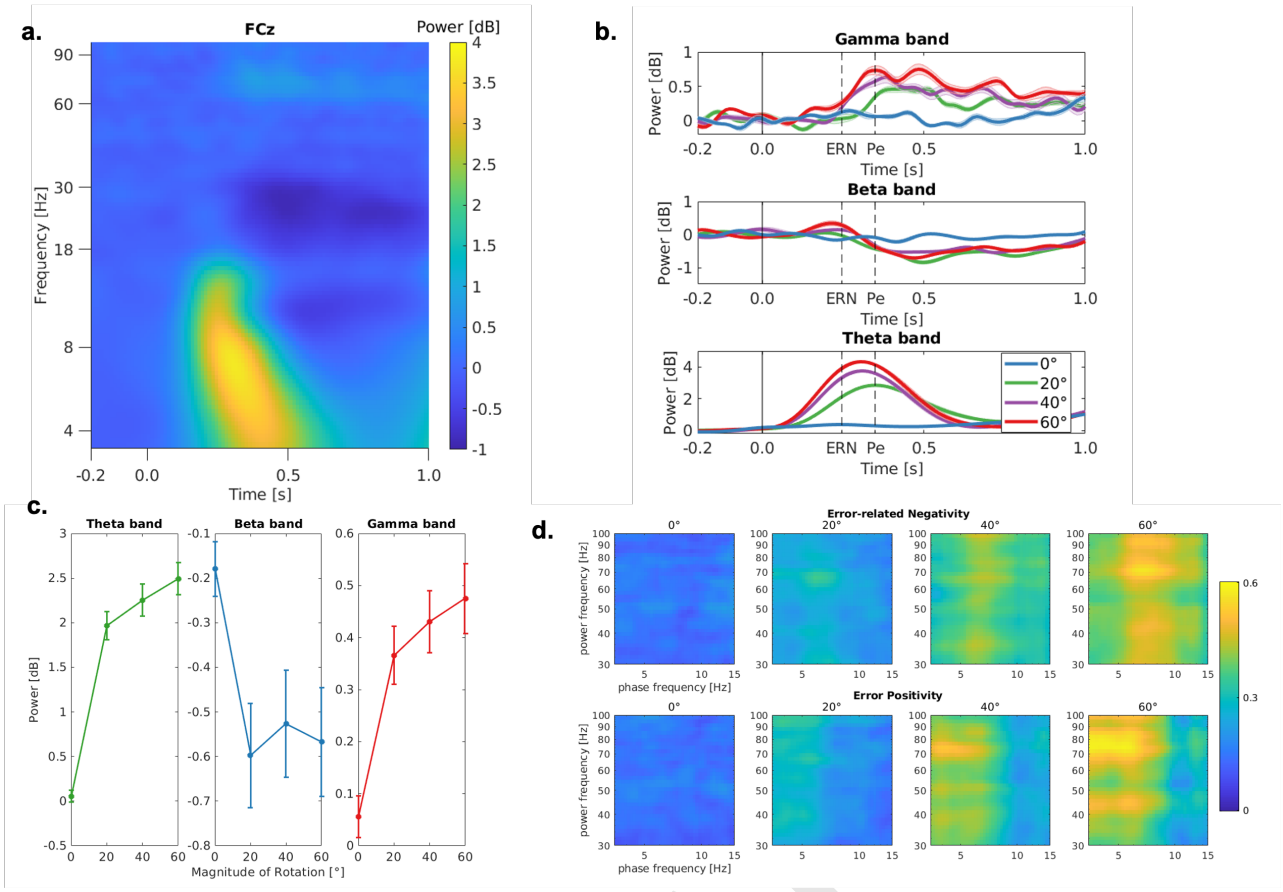

Fig. 2. Time-frequency representations of ErrPs at FCz electrode on session 1 and 2. **a.** Time-frequency decomposition of ErrPs averaged over the all rotation trials with respect to the onset of rotation. Power was normalized by pre-stimuli baseline ([-0.25, 0.0] s). **b.** Theta (4-8 Hz), beta (18-30 Hz) and gamma band (60-90 Hz) power modulation with respect to the onset of event ($x = 0\ s$) for each magnitude of rotation. Two dashed black lines at 0.25 s and 0.35 s indicate when ERN and Pe appeared. Theta band power increased within the time window of [0.1, 0.6] s with respect to the onset of rotation. Beta band power decreased, while gamma band power showed increase within the time window of [0.3, 0.8] s. **c.** Averaged band power modulation for each magnitude of rotation of session 1 and 2. Theta and gamma band power in erroneous trials were modulated as a function of magnitude of rotation (Pearson's correlation analysis, Theta: $r = 0.69$, $p < 0.001$, Gamma: $r = 0.39$, $p < 0.001$), while beta band activity remained stable for the different magnitudes of rotation (Pearson's correlation analysis, $r = 0.09$, $p = 0.41$). **d.** Theta-gamma phase-amplitude coupling at ERN and Pe. Note that levels of coupling is larger for trials with larger magnitude of rotations.

ual perceptual thresholds to detect a visuomotor rotation.

As illustrated in Fig. 1a, participants used a joystick to control a cursor to reach a target. Unlike typical visuomotor rotation tasks (33–36), the visuomotor coupling between the cursor movement and the joystick was disrupted during the continuous cursor controlling task occasionally and with varying magnitudes in order to ensure participants could predict cursor trajectories and, so, elicit ErrPs in their EEG. This design enabled to induce stable and precise perturbations on the cursor trajectory and associated corrective actions across sessions (Fig. 1c and d). Furthermore, the elicited ErrPs were also stable across the three recording sessions (Fig. 3), in line with previous findings (8, 18, 37). On average, 46 and 30 days elapsed between consecutive sessions, respectively (Table 2).

While most theories of performance monitoring consider ErrPs as a detector (38, 39), some studies found that ErrPs covary with the magnitude of errors (9, 10). However, these studies were limited to a short number of discrete error categories (i.e., small, medium and large), thus not capturing a continuous relationship between the two —which is crucial to explain our individual ability to detect errors. Moreover, whether or not ErrPs encode magnitude of errors has remained controversial, as other studies reported that different magnitudes of a visuomotor rotation do not affect ErrPs by comparing rotations of 45° and 180° (11). Our results extend and reconcile previous research as we have identified a continuous non-linear relationship between the magnitude of errors and the output of the ErrP-BCI, which starts plateauing after 30° of rotation (Fig. 4).

Having established this non-linear relationship, one fundamental question arises; namely, "Can we infer participants' perceptual threshold to detect errors?". As shown in Fig. 5a, behavioral answers to conscious perception of errors and inferred subjects' responses from ErrPs were similarly modulated along with the magnitude of rotation. Interestingly, we observed that even at the magnitude where participants were unsure about the presence of the rotation (i.e., "Maybe") the behavioral and inferred answers were closely aligned to each other. ErrPs for "Maybe" exhibited smaller and delayed deflections than for ErrPs elicited by conscious perception of the rotation (i.e., "Yes", Fig. 3c). Additionally, Fig. 5b revealed a significant correlation between the behavioral perceptual threshold, or inflection point, and the inferred per-

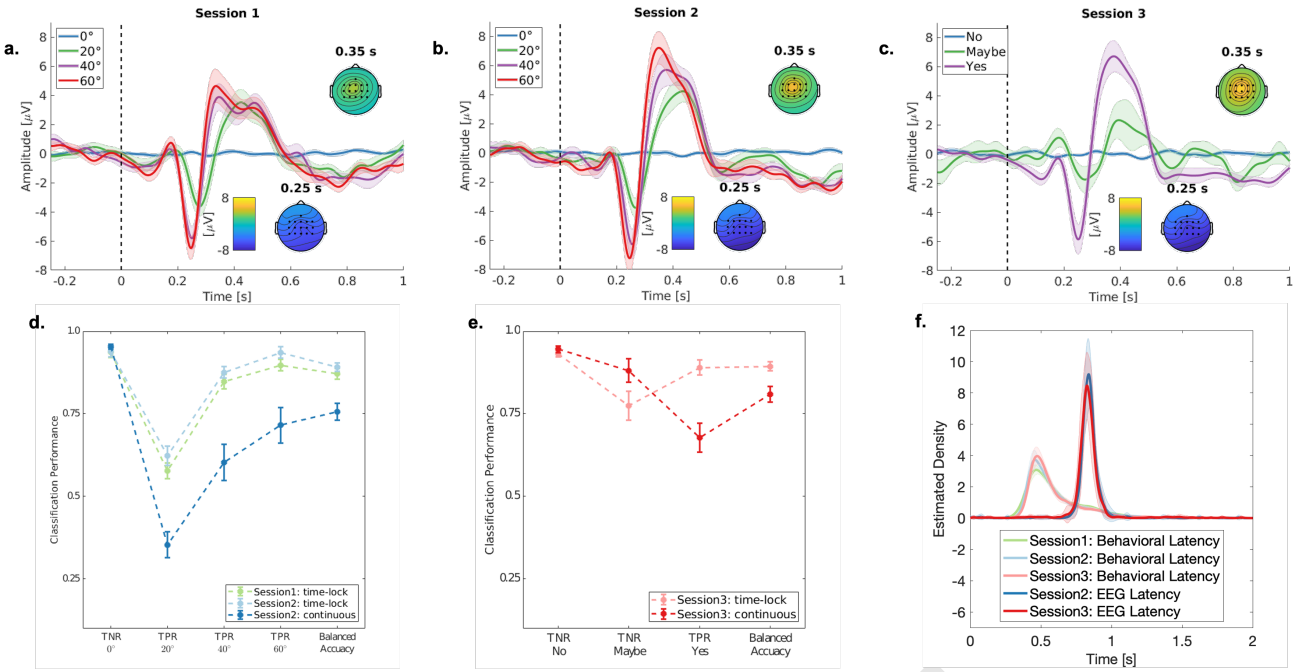

Fig. 3. Grand-averaged signals and classification performance. **a., b., c.** Grand-averaged signals at FCz channel for each recording session, respectively. The dashed line ($x = 0$ s) represents the onset of rotation. On the first and the second recording session, each line corresponds to a magnitude of rotation; while lines correspond to the subjective behavioral answers on the third session. Each panel includes topographical representations averaged over trials with rotation of the negative and positive deflections at 0.25 and 0.35 s. **d., e.** Classification performance for time-locked classification and continuous decoding on the first two sessions and the third session, respectively. Note that True positive rate (TPR) increased as a function of magnitude on session 1 and 2.

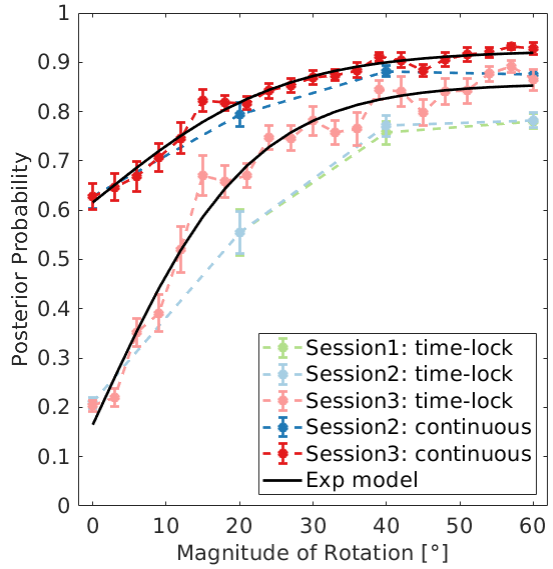

Fig. 4. Estimated posterior probabilities of each recording session for each magnitude of rotation and fitted curve for both time-lock classification and continuous decoding on session 3. Note that estimated posterior probability is modelled as an exponential function of the magnitude of rotation.

ceptual threshold. Taken together, our results suggests that ErrPs encode not only the magnitude of errors, but also the individual perceptual threshold to discern them consciously.

Our individual ability to detect errors of varying magnitudes is key to learn in motor adaptation tasks, where the cerebellum is known to play a major role (40–42). We speculate that neural correlates of error severity originate from Purkinje cells in the cerebellum and are projected onto the ACC via a cingulocerebellar circuit (43–45) to elicit ErrPs. In fact, the non-linear relationship between the magnitude of errors and the ErrP is consistent with non-human primate studies (46), in which monkeys manually tracked a pseudo-randomly moving target. Authors also found a non-linear relationship between size of errors and simple spike activity of Purkinje cells. Furthermore, patient studies seem to support that the cerebellum is involved in error processing (as reviewed in (47)) and there exists some evidence of cerebellar encoding of sensory prediction errors during motor tasks (48). Our experimental setup and findings open new avenues to probe and extend current theories of performance monitoring, which are based on response conflict tasks such as flanker (see, e.g., (38, 39) for reviews), by incorporating continuous human-interaction tasks as well as analysis of the ErrP complex as a whole rather than individual peaks. Moreover, while these theories interpret that the frontocentral Pe is simply associated with fast orienting and attentional processes, our results show Pe encodes qualitatively and quantitatively more information. In particular, while we observe a larger subsequent centropaerietal Pe at 400 ms (Fig S1), which has been proposed to drive adaptation (39), the two positive deflections reflect similarly the magnitude of errors.

Our results are not limited to the theta band activity of EEG. Völker et al. (17) recently reported the presence of the high-gamma band modulation during an Erikson flanker task in both invasive and noninvasive EEG recordings. High-gamma band ([60, 90] Hz) power increased when humans performed erroneous motor actions time-locked to the Pe component of ErrPs. Consistent with their findings, our results also demon-

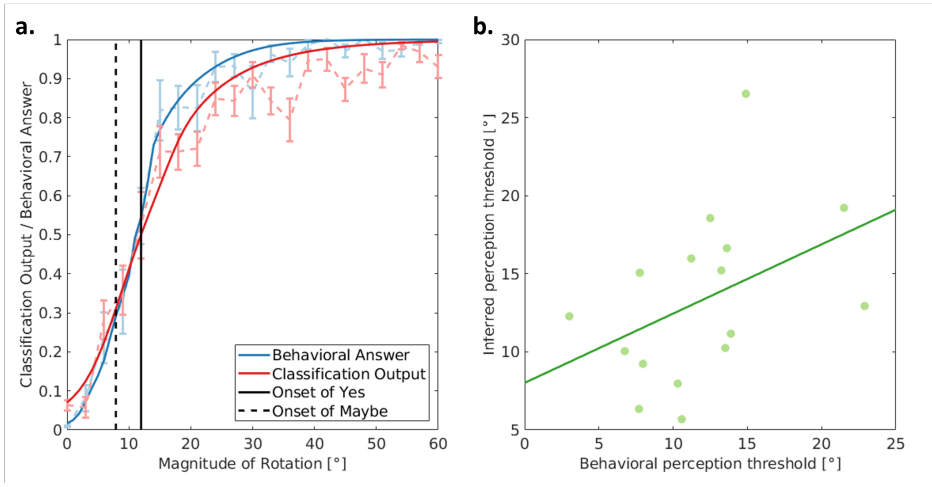

Fig. 5. Inferring each subject's individual perceptual threshold to detect a visuomotor rotation. **a.** Answer to the questionnaires collected after each trial and the results of the time-locked classification on the data collected on the third session. Black solid vertical line corresponds to onset of conscious perception (Yes) while black dashed line is onset of Maybe. For decoding output (red), 1 means that all trials were estimated as erroneous (there was a rotation), while 0 means that all trials were estimated as correct (no rotation). For behavioral answer (blue), 1 indicates that all trials of a given rotation was consciously perceived (i.e., Yes), while 0 means that all trials were not consciously perceived (i.e., Maybe or No). Behavioral answer and classification output increased similarly over the magnitude of rotation before and after the perceptual threshold (i.e., Onset of Yes). **b.** Scatter plot of the behavioral individual perceptual threshold and the inferred perceptual threshold based on the time-locked classification of ErrPs. Each dot corresponds to one subject. Green line corresponds to the regressed line by least-mean square.

strate that the peak high-gamma power aligns with the Pe deflection in the same high-gamma band ([60, 90] Hz, Fig. 2b). Extending their results, Fig. 2d illustrates an increase only in theta and gamma band power, but not in beta. Furthermore, we observed a theta-gamma phase-amplitude coupling, which has often been observed during sensory signal detection and visual perception tasks (49, 50) (Fig. 2c). Although we have further analyzed datasets collected during our previous studies (27, 29), we did not observe such gamma band activity nor theta-gamma phase-amplitude coupling. A distinction between those previous studies and the present study is that in the latter subjects performed corrective actions upon perception of an error. Indeed, Krigolson *et al.* (51) showed that "correctability" of the task influences theta band activity; however, how the "correctability" modulates gamma band activity remains unclear. Altogether, these results suggest that theta-gamma coupling may occur only in the case where corrective actions are necessary to accomplish the task and covaries with magnitude of the perceived errors.

This study also uncovered a tight temporal relationship between corrective actions and the two characteristic electrophysiological deflections of ErrPs; namely, ERN and Pe. As shown in Fig. 3, we observed ERN at 0.25 s with respect to the rotation onset, which corresponds to the time period where participants initiate the corrective actions to re-aim the target (Fig. 1d). Similarly, Pe was observed at 0.35 s, in the middle of corrective actions. Interestingly, temporal patterns of both joystick speed and high-gamma band power were monotonically increasing from baseline towards its peak value within the time window between ERN and Pe. Overall, our results suggest presence of rapid information transfer between theta and high-gamma band activity to activate corrective actions of right amount after detection of an error.

Finally, our study has implications for single-trial decoding of ErrPs during continuous human-computer interaction. The individual BCI decoders exhibited good transfer across recording sessions and scalability over the varying magnitude of errors. As shown in Fig. 3, stable ErrP patterns over the recording sessions enabled us to deploy "Plug-and-Play" ErrP-BCIs on the second and the third session, in which online decoding of ErrPs were carried out since the first run of the session by transferring the decoder from the previous recordings. Transfer learning to detect ErrPs has been investigated across different error types (52, 53), cognitive workload conditions (27, 54) and participants (25, 55); however, they often reported degraded classification performance. This was not the case in our experiments, where we observed consistent classification performance by transferring the personalized decoder over the different decoding sessions, especially during online continuous classification (Fig 3d and e, and Table 1). Nevertheless, our results revealed the difficulty to detect small errors compared to large ones due to the reduced amplitude and delayed deflections of their elicited ErrPs (Fig. 3a and b, and Fig. 4). Importantly, the latency to detect ErrPs was close to the optimal latency and very stable across sessions during online continuous decoding (Fig. 3f), thus demonstrating the temporal precision of the continuous ErrP-BCI. We conjecture that such a kind of ErrP-BCI could enhance operation of assistive devices by people with severe motor disabilities. Indeed, because of their degraded residual control, these subjects will occasionally deliver wrong commands similar to the visuomotor rotations in our experiments, and will not be fast enough to execute corrective actions before the output of the ErrP-BCI will be available.

Materials and Methods

Participants. Sixteen able-bodied healthy subjects (four female, 23 ± 1 years old) participated in the experiment, which consisted of three recording sessions (days). The experimen-

DRAFT

tal protocol was approved by the local ethics commission (PB_2017-00295). Written informed consent was collected from all participants before conducting the experiment. During the experiment, participants sat on a comfortable chair in front of a laptop with a 14-inch display that visualized the experimental protocol.

Experimental design. Fig. 1a illustrates the experimental protocol. A blue circle represented the cursor which was controlled by the left joystick of a game-pad (DualShock4, Sony, Japan), and a red square represented the goal location where participants were instructed to bring the cursor as quickly as possible. The speed of the cursor was kept constant (750 pixel/s) during the cursor reaching task as long as the joystick was pressed. Averaged duration of a trial was 3.5 ± 0.2 s. The goal location was randomly chosen for each trial among six potential locations; i.e., top-left, middle-left, low-left, top-right, middle-right and low-right. Initial position of the cursor was at the other side of the target at a random height to ensure enough distance (at least 1960 pixel) between the initial position of the cursor and the goal. For example, if the goal was on the right side, the cursor was placed on the left side at a random height and vice versa. In 30% of trials, the joystick-to-cursor mapping was rotated when the cursor exceeded a pre-defined invisible boundary. The boundary was randomly determined for each trial. Trials with a visuomotor rotation were defined as "erroneous trials", and others as "correct trials". The magnitude of rotation was fixed to $20°$, $40°$ and $60°$ on the first and the second sessions. On the third session, the magnitude of rotation was between $3°$ to $60°$ with a step of $3°$, and after each trial participants were asked whether they perceived the rotation, maybe or not. Table 2 reports the days difference between each recording session for each subject.
As illustrated in Fig. 1b subjects performed 10 runs of 40 trials in each session (400×3 trials in total). Before these runs, participants made eye movements for 90 s for estimating regression parameters to remove EOG artifacts from their EEG during the actual experiment (56).
Participants executed the experiment without receiving online feedback on the first session. We provided subjects with online feedback on the second and the third sessions by changing the color of the cursor upon ErrP detection. On the second session, presence of ErrPs was continuously monitored during cursor control, and the decoder was re-calibrated after each run. On the third session, we carried out continuous decoding of ErrPs without re-calibrating the decoder, which was built with data from the first and the second sessions, except for the parameters to remove EOG artifact.

EEG and EOG acquisition. 16 EEG and 3 EOG electrodes were recorded throughout the experiment (two synchronized g.USBAmp, g.tec medical engineering, Austria). EEG electrodes were located at Fz, FC3, FC1, FCz, FC2, FC4, C3, C1, Cz, C2, C4, CP3, CP1, CPz, CP2 and CP4 in 10/10 international coordinates, and EOG electrodes were placed at above the nasion and below the outer canthi of the eyes. The ground electrode was placed on the forehead (AFz) and the reference electrode was placed on the left earlobe. We used the same reference and ground electrode for both EEG and EOG signals. EEG and EOG signals were notch filtered at 50 Hz by the amplifiers. To reduce signal contamination, participants were asked to avoid excessive eye movements and blinks during trials.

Time-frequency analysis. To characterize the time-frequency representation of ErrPs elicited by visuomotor rotations, we computed a discrete wavelet time-frequency decomposition (57). After applying a 2nd order non-causal high-pass Buttterworth filter with the cut-off frequency of 1 Hz and current source density (CSD), EEG signals were epoched in the time window [-0.2, 1.0] s with respect to the onset of rotations. For each single-trial EEG epoch we performed the Morlet Wavelet time-frequency decomposition (58) in the frequency range [3, 100] Hz, resulting in a wavelet coefficient matrix with 126 time points and 97 log-spaced frequency bins. Each of time windows were composed of 427 samples (0.83 s) overlapped by 51 samples (0.1 s); while the number of cycles ranges from 3 to 20 at highest. The resulting coefficients were used to extract spectral power and phase-amplitude coupling.
To compute the spectral power induced by a visuomotor rotation we used the event-related spectral perturbation (ERSP) approach (59). This approach is less sensitive to noisy trials than classical baseline correction methods, and produces a non-skewed power distribution. In detail, separately for each subject and experimental condition, we apply a single-trial full-epoch baseline correction, before averaging across trials and removing the trial-averaged pre-stimulus (i.e., from -0.25 to 0.0 s) baseline. Baselines were corrected using the gain model assumption (i.e., divide by the baseline) instead of the additive model (i.e., subtract the baseline) (59, 60). Finally, the trial-averaged pre-stimulus corrected time frequency coefficients were log-transformed ($10\log_{10}$).
To compute the phase-amplitude coupling, we first identified the latency of ERN and Pe (0.25 and 0.35 ms, respectively), then used the mean vector length (MVL) method. MVL has been reported to be more suitable for high signal-to-noise ratio data as it is more sensitive to coupling strength and width compared to other methods such as modulation index or phase-locking value (61). This method estimates the coupling between phase frequency f_p and amplitude frequency f_a from a number of epochs N, by mapping phase time series $\phi_{f_p}(t,n)$ and amplitude time series $A_{f_a}(t,n)$ to a complex-values vector at each time point, t, and each epoch, n. To quantify the coupling between f_p and f_a, the MVL method measures the length of the average vector and computes phase amplitude coupling as follows:

$$MVL(f_a, f_p) = |\frac{1}{N}\sum_{n=1}^{N} A_{f_a}(t,n)\exp^{j\phi_{f_p}(t,n)}| \quad \textbf{(1)}$$

.

BCI Decoding analysis. EEG signals were band-pass filtered with a 4th order causal Butterworth filter with cutoff frequencies of [1, 10] Hz, for both online and offline analyses.

DRAFT

Table 2. Time differences in days between the three recording sessions.

Subject ID	s1	s2	s3	s4	s5	s6	s7	s8	s9	s10	s11	s12	s13	s14	s15	s16	Mean ± SE
Session1 - Session 2	52	63	42	42	51	49	56	56	51	59	43	44	35	24	35	37	46 ± 3
Session2 - Session 3	25	13	40	35	38	38	28	31	26	11	32	45	52	32	21	10	30 ± 3

To build the individual decoders, ErrPs were segmented into epochs in the time window of [0.2, 0.8] s with respect to the onset of the visuomotor rotation. Firstly, to enhance the signal-to-noise ratio of the EEG, we applied a spatial filter based on canonical correlation analysis (CCA) (37, 62). This spatial filter method transforms the averaged ErrPs to a subspace containing different ERP components (63). Only the first three components were kept for the subsequent analysis. This number was determined based on the data collected on the first session by performing pseudo-continuous decoding in cross validation. For every trial, we extracted three complementary types of features: the decimated signal amplitude per CCA component at 64 Hz; power spectral densities per CCA component from 4 to 10 Hz with a step of 2 Hz; and the covariance matrix on Riemannian geometry, which computes a low-dimensionality manifold representation from a non-linear combination of the EEG component space (64). In order to include information of the EEG temporal dynamics in the Riemannian spatial covariance matrix, the epoch X was augmented with an individual template T representing the grand average of erroneous trials in the training set:

$$Z = [X \;\; T] \tag{2}$$

$$C_Z = \frac{1}{s} Z^T Z = \frac{1}{s} \begin{pmatrix} X^T X & X^T T \\ T^T x & T^T T \end{pmatrix} \tag{3}$$

where s denotes number of time samples of an epoch. The covariance between X and T allows to capture the temporal dynamics of multi-component EEG signals with respect to the template. The covariance matrix was then projected on the tangent space, computed only on the training dataset (65). All computed features were concatenated and normalized within the range of [0, 1]. From this feature vector $\mathbf{x}$, we computed the estimated posterior probability of having detected an error, $p(error|\mathbf{x})$ using diagonal linear discriminant analysis (LDA):

$$p(error|\mathbf{x}) = \frac{1}{1 - \exp^{-(\mathbf{w}'\mathbf{x}+b)}} \tag{4}$$

In order to continuously monitor the presence or absence of ErrPs, we analyzed the EEG signal with a sliding window, online or offline (24, 27).

To compute the estimated posterior probability of the training data without overfitting, aforementioned signal processing was performed in a leave-one-run-out cross-validation manner. Training folds were used to create an ErrP decoder, while the testing fold was used to compute the continuous modulation of posterior probability during cursor control with a sliding window at 32 Hz, 16 sample shift. In order to infer participants' erroneous perception in a continuous manner and provide them with the feedback upon the detection of ErrPs, two hyperparameters were optimized besides the ErrP decoder; namely, smoothing factor and decision threshold. The smoothing factor indicates length of the time window for an online moving average filter on the estimated posterior probabilities, ranging from 1 to 16 with a step of 1. The decision threshold determined presence or absence of erroneous perception, ranging from 0 to 1 with a step of 0.01. Hyperparameter optimization was carried out in a grid search manner. Specifically, we computed the Matthew's correlation coefficient (MCC) for each pair of hyperparameters based on a confusion matrix. With a pair of hyperparameters, a correct trial was properly classified if the smoothed posterior probability did not exceed the decision threshold (True Negative). If the smoothed posterior probability in a correct trial exceeded the decision threshold, the trial was considered as erroneous (False Positive). On the other hand, an erroneous trial was correctly classified if the posterior probability exceeded the decision threshold in a time window of [0.5, 1.1] s with respect to the onset of the rotation (True Positive). This time window of [0.5, 1.1] s was determined as the optimal latency was 0.8 s and we allowed 0.3 s of temporal difference with respect to the optimal latency. If the averaged posterior probability in an erroneous trial exceeded the decision threshold outside the aforementioned time window or did not exceed the decision threshold, it was considered as wrong classification (False Negative). For each pair of hyperparameters we computed their MCC, a 16 × 101 matrix for each testing fold. The pair of hyperparameters with the highest MCC, averaged over the testing folds, was chosen as the optimal. Once the pair of optimal hyperparameters was determined, we used all the available data to re-compute the ErrP decoder to be deployed subsequently for online continuous decoding. Decoder re-calibrations during the second session—from runs 2 to 10—used the all available data up to that moment (i.e., first session plus previous runs in second session), and re-estimated the pair of optimal hyperparameters. On the second and the third sessions, we provided participants with the online feedback when the smoothed posterior probability exceeded the decision threshold for the first time in a trial.

Individual perception threshold. In order to model behavioral perception and estimated posterior probabilities over the magnitudes of rotation (Fig. 5), we used the following exponential function:

$$y = k_1 + k_2(1 - \exp^{-k_3(x-k_4)}) \tag{5}$$

where k_{1-4} represent the initial value, maximum value, magnitude of slope and inflection point of the curve, respectively; and x represents the magnitude of rotation. Parameter k_{1-4} were estimated by gradient descent with the objective function defined as the root mean square error between the observation and the fitted model.

DRAFT

ACKNOWLEDGEMENTS
This work was supported by the Hasler Foundation, Switzerland.

Bibliography

1. PM A Rabbitt. Errors and error correction in choice-response tasks. *Journal of Experimental Psychology*, 71(2):264, 1966.
2. Rachael D. Seidler, Ajitkumar P. Mulavara, Jacob J. Bloomberg, and Brian T. Peters. Individual predictors of sensorimotor adaptability. *Frontiers in Systems Neuroscience*, 9, 2015. ISSN 1662-5137. doi: 10.3389/fnsys.2015.00100.
3. R. D. Seidler and R. G. Carson. Sensorimotor learning: Neurocognitive mechanisms and individual differences. *Journal of Neuroengineering and Rehabilitation*, 14(1):74, Jul 2017. ISSN 1743-0003. doi: 10.1186/s12984-017-0279-1.
4. William J. Gehring, Brian Goss, Michael G. H. Coles, David E. Meyer, and Emanuel Donchin. A neural system for error detection and compensation. *Psychological Science*, 4 (6):385–390, 2021/01/26/ 1993.
5. Michael Falkenstein, Jörg Hoormann, Stefan Christ, and Joachim Hohnsbein. ERP components on reaction errors and their functional significance: A tutorial. *Biological Psychology*, 51(2):87 – 107, 2000. doi: https://doi.org/10.1016/S0301-0511(99)00031-9.
6. Markus Ullsperger and D Yves Von Cramon. Subprocesses of performance monitoring: A dissociation of error processing and response competition revealed by event-related fMRI and ERPs. *Neuroimage*, 14(6):1387–1401, 2001.
7. Hein T van Schie, Rogier B Mars, Michael GH Coles, and Harold Bekkering. Modulation of activity in medial frontal and motor cortices during error observation. *Nature Neuroscience*, 7(5):549–554, 2004.
8. Ricardo Chavarriaga, Aleksander Sobolewski, and José del R. Millán. Errare machinale est: The use of error-related potentials in brain-machine interfaces. *Frontiers in Neuroscience*, 8:208, 2014. doi: 10.3389/fnins.2014.00208.
9. Holger Hill. An event-related potential evoked by movement planning is modulated by performance and learning in visuomotor control. *Experimental Brain Research*, 195(4):519–529, Jun 2009. doi: 10.1007/s00221-009-1821-6.
10. G. Spinelli, G. Tieri, E.F. Pavone, and S.M. Aglioti. Wronger than wrong: Graded mapping of the errors of an avatar in the performance monitoring system of the onlooker. *NeuroImage*, 167:1–10, 2018. ISSN 1053-8119.
11. Martin Spüler and Christian Niethammer. Error-related potentials during continuous feedback: Using EEG to detect errors of different type and severity. *Frontiers in Human Neuroscience*, 9:155, 2015. doi: 10.3389/fnhum.2015.00155.
12. R. Chavarriaga and José del R Millán. Learning from EEG error-related potentials in noninvasive brain-computer interfaces. *IEEE Transactions on Neural Systems and Rehabilitation Engineering*, 18(4):381–388, Aug 2010. doi: 10.1109/TNSRE.2010.2053387.
13. Milan Brázdil, Robert Roman, Michael Falkenstein, Pavel Daniel, Pavel Jurák, and Ivan Rektor. Error processing–evidence from intracerebral ERP recordings. *Experimental Brain Research*, 146(4):460–466, 2002.
14. Vincent Van Veen and Cameron S Carter. The anterior cingulate as a conflict monitor: fMRI and ERP studies. *Physiology & Behavior*, 77(4-5):477–482, 2002.
15. Martin J Herrmann, Josefine Römmler, Ann-Christine Ehlis, Anke Heidrich, and Andreas J Fallgatter. Source localization (LORETA) of the error-related-negativity (ERN/Ne) and positivity (Pe). *Cognitive Brain Research*, 20(2):294–299, 2004.
16. Gezelle Dali, Méadhbh Brosnan, Jeggan Tiego, Beth P Johnson, Alex Fornito, Mark A Bellgrove, and Robert Hester. Examining the neural correlates of error awareness in a large fMRI study. *Cerebral Cortex*, 2022. ISSN 1047-3211. doi: 10.1093/cercor/bhac077. bhac077.
17. Martin Völker, Lukas D.J. Fiederer, Sofie Berberich, Jiří Hammer, Joos Behncke, Pavel Kršek, Martin Tomášek, Petr Marusič, Peter C. Reinacher, Volker A. Coenen, Moritz Helias, Andreas Schulze-Bonhage, Wolfram Burgard, and Tonio Ball. The dynamics of error processing in the human brain as reflected by high-gamma activity in noninvasive and intracranial EEG. *NeuroImage*, 173:564–579, 2018. doi: https://doi.org/10.1016/j.neuroimage.2018.01.059.
18. P. W. Ferrez and José del R Millán. Error-related EEG potentials generated during simulated brain-computer interaction. *IEEE Transactions on Biomedical Engineering*, 55(3):923–929, March 2008. doi: 10.1109/TBME.2007.908083.
19. Pierre W Ferrez and José del R Millán. Simultaneous real-time detection of motor imagery and error-related potentials for improved BCI accuracy. In *Proceedings of the 4th International Brain-Computer Interface Workshop and Training Course*, pages 197–202, 2008.
20. Martin Spüler, Michael Bensch, Sonja Kleih, Wolfgang Rosenstiel, Martin Bogdan, and Andrea Kübler. Online use of error-related potentials in healthy users and people with severe motor impairment increases performance of a P300-BCI. *Clinical Neurophysiology*, 123(7):1328 – 1337, 2012. doi: https://doi.org/10.1016/j.clinph.2011.11.082.
21. Nico M. Schmidt, Benjamin Blankertz, and Matthias S. Treder. Online detection of error-related potentials boosts the performance of mental typewriters. *BMC Neuroscience*, 13(1): 19, Feb 2012. doi: 10.1186/1471-2202-13-19.
22. I Iturrate, Ricardo Chavarriaga, Luis Montesano, Javier Minguez, and José del R. Millán. Teaching brain-machine interfaces as an alternative paradigm to neuroprosthetics control. *Scientific Reports*, 5(13893):10, 2015.
23. A. F. Salazar-Gomez, J. DelPreto, S. Gil, F. H. Guenther, and D. Rus. Correcting robot mistakes in real time using EEG signals. In *2017 IEEE International Conference on Robotics and Automation*, pages 6570–6577, May 2017. doi: 10.1109/ICRA.2017.7989777.
24. Catarina Lopes-Dias, Andreea I. Sburlea, and Gernot R. Müller-Putz. Online asynchronous decoding of error-related potentials during the continuous control of a robot. *Scientific Reports*, 9(1):17596, 2019. doi: 10.1038/s41598-019-54109-x.
25. Catarina Lopes-Dias, Andreea I. Sburlea, Katharina Breitegger, Daniela Wyss, Harald Drescher, Renate Wildburger, and Gernot R. Müller-Putz. Online asynchronous detection of error-related potentials in participants with a spinal cord injury using a generic classifier. *Journal of Neural Engineering*, 18(4):046022, Mar 2021. doi: 10.1088/1741-2552/abd1eb.
26. Jason Omedes, I Iturrate, Javier Minguez, and Luis Montesano. Analysis and asynchronous detection of gradually unfolding errors during monitoring tasks. *Journal of Neural Engineering*, 12(5):056001, 2015.
27. Fumiaki Iwane, I naki Iturrate, Ricardo Chavarriaga, Lucian Gheorghe, and José del R Millán. Invariability of EEG error-related potentials during continuous feedback protocols elicited by erroneous actions at predicted or unpredicted states. *Journal of Neural Engineering*, 18(4):046044, 2021.
28. I Iturrate, Jonathan Grizou, Jason Omedes, Pierre-Yves Oudeyer, Manuel Lopes, and Luis Montesano. Exploiting task constraints for self-calibrated brain-machine interface control using error-related potentials. *PLoS ONE*, 10:1–15, 07 2015. doi: 10.1371/journal.pone.0131491.
29. Iason Batzianoulis, Fumiaki Iwane, Shupeng Wei, Carolina Gaspar Pinto Ramos Correia, Ricardo Chavarriaga, José del R. Millán, and Aude Billard. Customizing skills for assistive robotic manipulators, an inverse reinforcement learning approach with error-related potentials. *Communications Biology*, 4(1):1406, Dec 2021. ISSN 2399-3642. doi: 10.1038/s42003-021-02891-8.
30. Daniel B Silversmith, Reza Abiri, Nicholas F Hardy, Nikhilesh Natraj, Adelyn Tu-Chan, Edward F Chang, and Karunesh Ganguly. Plug-and-play control of a brain-computer interface through neural map stabilization. *Nature Biotechnology*, 39:326–335, 2021.
31. Amirhossein Jahani, Antoine Schwey, Pierre-Michel Bernier, and Nicole Malfait. Spatially distinct beta-band activities reflect implicit sensorimotor adaptation and explicit re-aiming strategy. *Journal of Neuroscience*, 40(12):2498–2509, 2020. ISSN 0270-6474. doi: 10.1523/JNEUROSCI.1862-19.2020.
32. Julie Alayrangues, Flavie Torrecillos, Amirhossein Jahani, and Nicole Malfait. Error-related modulations of the sensorimotor post-movement and foreperiod beta-band activities arise from distinct neural substrates and do not reflect efferent signal processing. *NeuroImage*, 184:10–24, 2019. ISSN 1053-8119. doi: https://doi.org/10.1016/j.neuroimage.2018.09.013.
33. Helen A Cunningham. Aiming error under transformed spatial mappings suggests a structure for visual-motor maps. *Journal of Experimental Psychology: Human Perception and Performance*, 15(3):493–506, 1989.
34. Mark R. Hinder, James R. Tresilian, Stephan Riek, and Richard G. Carson. The contribution of visual feedback to visuomotor adaptation: How much and when? *Brain Research*, 1197: 123–134, 2008. ISSN 0006-8993.
35. Mark R. Hinder, Stephan Riek, James R. Tresilian, Aymar de Rugy, and Richard G. Carson. Real-time error detection but not error correction drives automatic visuomotor adaptation. *Experimental Brain Research*, 201(2):191–207, Mar 2010. ISSN 1432-1106. doi: 10.1007/s00221-009-2025-9.
36. Miri Benyamini, Igor Demchenko, and Miriam Zacksenhouse. Error related EEG potentials evoked by visuo-motor rotations. *Brain Research*, 1769:147606, 2021. ISSN 0006-8993. doi: https://doi.org/10.1016/j.brainres.2021.147606.
37. Fumiaki Iwane, Ricardo Chavarriaga, I Iturrate, and José del R. Millán. Spatial filters yield stable features for error-related potentials across conditions. In *IEEE International Conference on Systems, Man, and Cybernetics*, pages 661–666, 2016.
38. Markus Ullsperger, Claudia Danielmeier, and Gerhard Jocham. Neurophysiology of performance monitoring and adaptive behavior. *Physiological Reviews*, 94(1):35–79, 2014.
39. Markus Ullsperger, Adrian G Fischer, Roland Nigbur, and Tanja Endrass. Neural mechanisms and temporal dynamics of performance monitoring. *Trends in Cognitive Sciences*, 18 (5):259–267, 2014.
40. Jessica Bernard and Rachael Seidler. Cerebellar contributions to visuomotor adaptation and motor sequence learning: An ALE meta-analysis. *Frontiers in Human Neuroscience*, 7, 2013. ISSN 1662-5161. doi: 10.3389/fnhum.2013.00027.
41. Elinor Tzvi, Leila Gajiyeva, Laura Bindel, Gesa Hartwigsen, and Joseph Classen. Coherent theta oscillations in the cerebellum and supplementary motor area mediate visuomotor adaptation. *NeuroImage*, 251:118985, 2022. ISSN 1053-8119. doi: https://doi.org/10.1016/j.neuroimage.2022.118985.
42. Elinor Tzvi, Sebastian Loens, and Opher Donchin. Mini-review: The role of the cerebellum in visuomotor adaptation. *The Cerebellum*, 21(2):306–313, Apr 2022. ISSN 1473-4230. doi: 10.1007/s12311-021-01281-4.
43. Jin Fan, Patrick R Hof, Kevin G Guise, John A Fossella, and Michael I Posner. The functional integration of the anterior cingulate cortex during conflict processing. *Cerebral Cortex*, 18 (4):796–805, 2008.
44. Peter L Strick, Richard P Dum, and Julie A Fiez. Cerebellum and nonmotor function. *Annual Review of Neuroscience*, 32:413–434, 2009.
45. Krystal L Parker, Nandakumar S Narayanan, and Nancy C Andreasen. The therapeutic potential of the cerebellum in schizophrenia. *Frontiers in Systems Neuroscience*, 8:163, 2014.
46. Laurentiu S. Popa, Angela L. Hewitt, and Timothy J. Ebner. Predictive and feedback performance errors are signaled in the simple spike discharge of individual purkinje cells. *Journal of Neuroscience*, 32(44):15345–15358, 2012. ISSN 0270-6474. doi: 10.1523/JNEUROSCI.2151-12.2012.
47. Jutta Peterburs and John E Desmond. The role of the human cerebellum in performance monitoring. *Current Opinion in Neurobiology*, 40:38–44, 2016.
48. John Schlerf, Richard B Ivry, and Jörn Diedrichsen. Encoding of sensory prediction errors in the human cerebellum. *Journal of Neuroscience*, 32(14):4913–4922, 2012.
49. Charles E. Schroeder and Peter Lakatos. Low-frequency neuronal oscillations as instruments of sensory selection. *Trends in Neurosciences*, 32(1):9–18, 2009. ISSN 0166-2236. doi: https://doi.org/10.1016/j.tins.2008.09.012.
50. Barbara Händel and Thomas Haarmeier. Cross-frequency coupling of brain oscillations indicates the success in visual motion discrimination. *NeuroImage*, 45(3):1040–1046, 2009. ISSN 1053-8119. doi: https://doi.org/10.1016/j.neuroimage.2008.12.013.
51. Olav E. Krigolson, Clay B. Holroyd, Geraldine Van Gyn, and Mathew Heath. Electroencephalographic correlates of target and outcome errors. *Experimental Brain Research*, 190 (4):401–411, Oct 2008. doi: 10.1007/s00221-008-1482-x.
52. Su Kyoung Kim and Elsa Andrea Kirchner. Classifier transferability in the detection of error related potentials from observation to interaction. In *2013 IEEE International Conference on Systems, Man, and Cybernetics*, pages 3360–3365, 2013. doi: 10.1109/SMC.2013.573.

DRAFT

53. Stefan K. Ehrlich and Gordon Cheng. A feasibility study for validating robot actions using EEG-based error-related potentials. *International Journal of Social Robotics*, 11(2):271–283, Apr 2019. doi: 10.1007/s12369-018-0501-8.
54. I Iturrate, R Chavarriaga, L Montesano, J Minguez, and José del R Millán. Latency correction of event-related potentials between different experimental protocols. *Journal of Neural Engineering*, 11(3):036005, 2014.
55. C. Lopes-Dias, A. I. Sburlea, and G. R. Müller-Putz. A generic error-related potential classifier offers a comparable performance to a personalized classifier. In *2020 42nd Annual International Conference of the IEEE Engineering in Medicine Biology Society (EMBC)*, pages 2995–2998, 2020. doi: 10.1109/EMBC44109.2020.9176640.
56. A. Schlögl, C. Keinrath, D. Zimmermann, R. Scherer, R. Leeb, and G. Pfurtscheller. A fully automated correction method of EOG artifacts in EEG recordings. *Clinical Neurophysiology*, 118(1):98 – 104, 2007. ISSN 1388-2457. doi: 10.1016/j.clinph.2006.09.003.
57. I Daubechies. The wavelet transform, time-frequency localization and signal analysis. *IEEE Transactions on Information Theory*, 36(5):961–1005, 1990. doi: 10.1109/18.57199.
58. Arnaud Delorme and Scott Makeig. EEGLAB: An open source toolbox for analysis of single-trial EEG dynamics including independent component analysis. *Journal of Neuroscience Methods*, 134(1):9–21, 2004. doi: 10.1016/j.jneumeth.2003.10.009.
59. Romain Grandchamp and Arnaud Delorme. Single-trial normalization for event-related spectral decomposition reduces sensitivity to noisy trials. *Frontiers in Psychology*, 2:236, 2011. doi: 10.3389/fpsyg.2011.00236.
60. Fumiaki Iwane, Giuseppe Lisi, and Jun Morimoto. EEG sensorimotor correlates of speed during forearm passive movements. *IEEE Transactions on Neural Systems and Rehabilitation Engineering*, 27(9):1667–1675, 2019. doi: 10.1109/TNSRE.2019.2934231.
61. Mareike J. Hülsemann, Ewald Naumann, and Björn Rasch. Quantification of phase-amplitude coupling in neuronal oscillations: Comparison of phase-locking value, mean vector length, modulation index, and generalized-linear-modeling-cross-frequency-coupling. *Frontiers in Neuroscience*, 13, 2019. ISSN 1662-453X. doi: 10.3389/fnins.2019.00573.
62. M. Spüler, A. Walter, W. Rosenstiel, and M. Bogdan. Spatial filtering based on canonical correlation analysis for classification of evoked or event-related potentials in EEG data. *IEEE Transactions on Neural Systems and Rehabilitation Engineering*, 22(6):1097–1103, Nov 2014. doi: 10.1109/TNSRE.2013.2290870.
63. Martin Spüler. Spatial filtering of EEG as a regression problem. In *7th Graz Brain-Computer Interface Conference*, 2017.
64. Marco Congedo, Alexandre Barachant, and Rajendra Bhatia. Riemannian geometry for EEG-based brain-computer interfaces; a primer and a review. *Brain-Computer Interfaces*, 4 (3):155–174, 2017.
65. A. Barachant, S. Bonnet, M. Congedo, and C. Jutten. Multiclass brain–computer interface classification by Riemannian geometry. *IEEE Transactions on Biomedical Engineering*, 59 (4):920–928, 2012.

DRAFT